Supplementary Information

Ultracompact On-chip Coiled Waveguide-Integrated Photodetectors Enabled by 2D materials with Enhanced Responsivity

Maaz Ahmed Qureshi,*[a‡] Fooqia Khalid,[b‡] Janvit Tippinit,[a] Faisal Ahmed,[b] Md Gius Uddin,[b] Abde Mayeen Shafi,[b] Xiaoqi Cui,[b] Matthieu Roussey,[a] Harri Lipsanen,[b] Zhipei Sun,[b] and Markku Kuittinen[a]

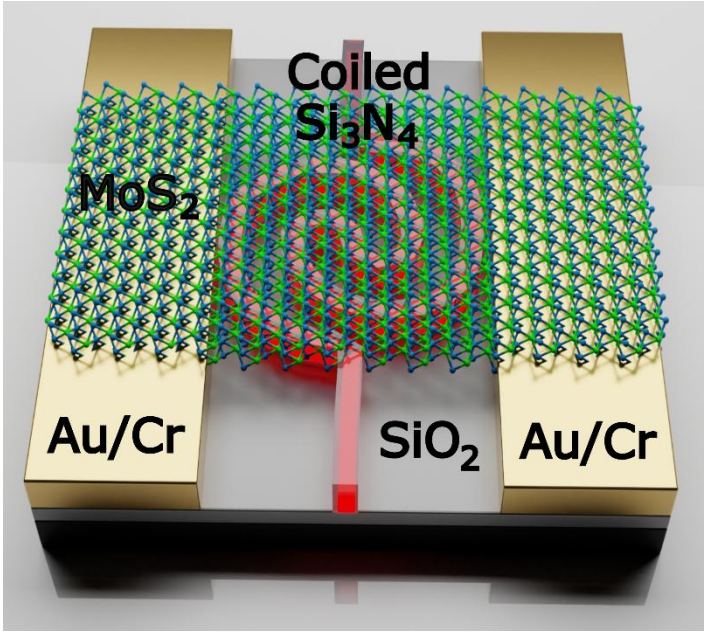

[a] Center for Photonics, University of Eastern Finland, Joensuu, Finland.
Email: maaz.qureshi@uef.fi, markku.kuittinen@uef.fi

[b] Department of Electronics and Nanoengineering, Aalto University, Espoo FI-02150, Finland.
Email: faisal.ahmed@aalto.fi, zhipei.sun@aalto.fi

* Corresponding author

‡ Contributed equally

Table of Contents

S1: Thickness dependence of MoS_2 on optical mode profile, transmittance, absorption.

Fig. S1a: Effect of MoS_2 thickness on optical mode confinement in the waveguide-integrated structure.

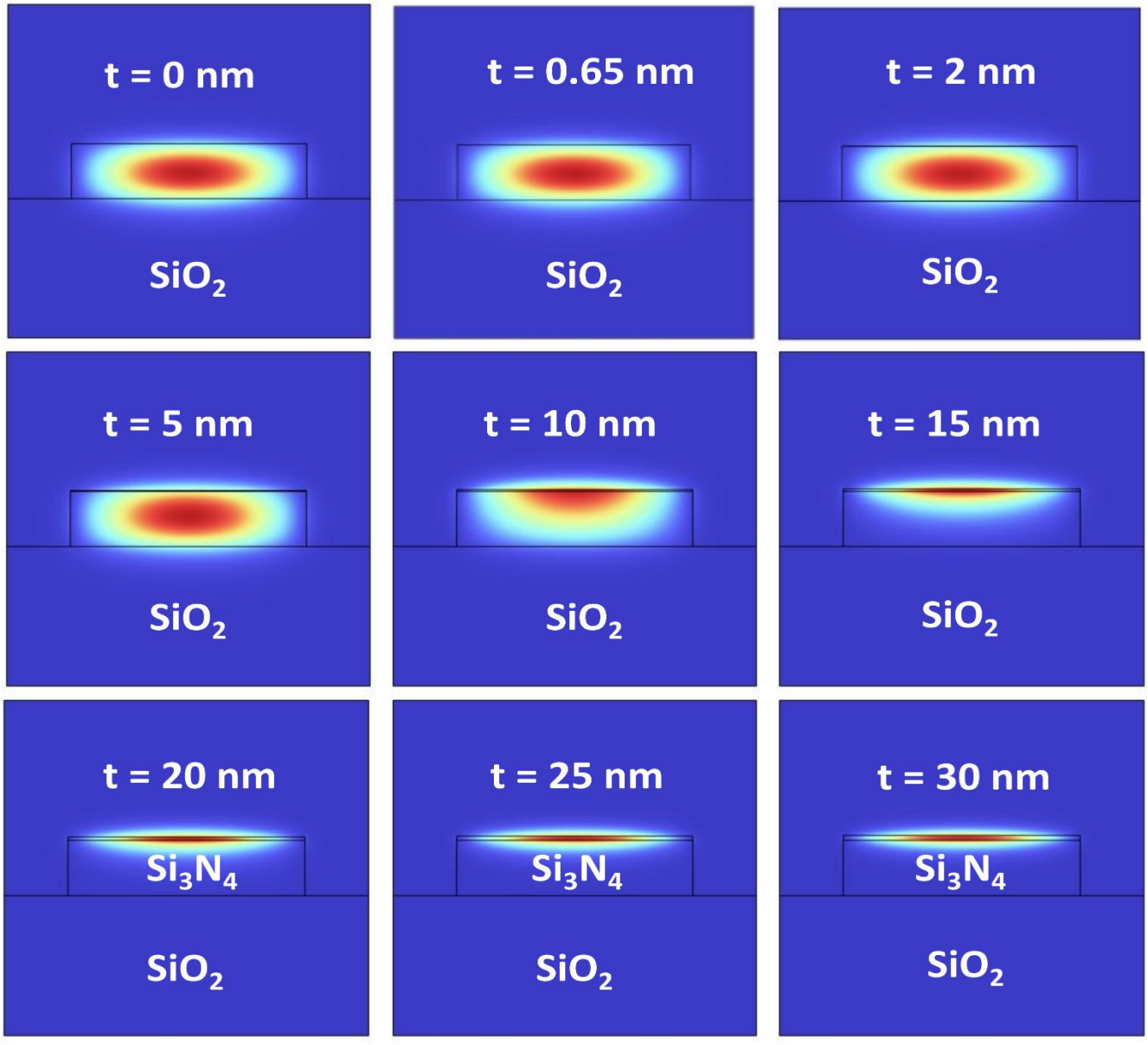

Figure S1a: Simulated optical mode profiles in a Si_3N_4 waveguide with varying MoS_2 film thicknesses from 0 to 30 nm. As the MoS_2 thickness increases, the optical mode gradually shifts upward and becomes more confined in the MoS_2 layer due to its higher refractive index. This enhanced light confinement in thicker MoS_2 layers leads to increased absorption, which directly influences photocurrent generation and responsivity. The simulations clearly visualize the evolution of mode distribution as a function of MoS_2 film thickness.

Fig. S1b: Simulated confinement and optical loss versus MoS_2 thickness on a Si_3N_4 waveguide.

Thickness of MoS_2 film (t [nm])	Confinement Factor (%)		Attenuation constant (dB/μm)
	Si_3N_4 waveguide	MoS_2 film	
0	100	0	0.05
5	93.75	0.71	0.96
10	82.84	5.32	6.44
15	61.47	17.39	23.50
20	47.15	29.92	36.28
25	37.58	41.10	45.33
30	30.51	50.69	51.71

Figure S1b: Simulated optical confinement factors and attenuation constant as a function of MoS_2 film thickness integrated on a Si_3N_4 waveguide. As the MoS_2 thickness increases from 0 to 30 nm, the optical mode increasingly shifts from the waveguide core to the MoS_2 layer, resulting in a significant rise in the confinement factor within MoS_2 and a corresponding increase in optical attenuation (from 0.05 to 51.71 dB/μm).

Fig. S1c: Simulated confinement factors and optical loss versus MoS_2 thickness on a Si_3N_4 waveguide.

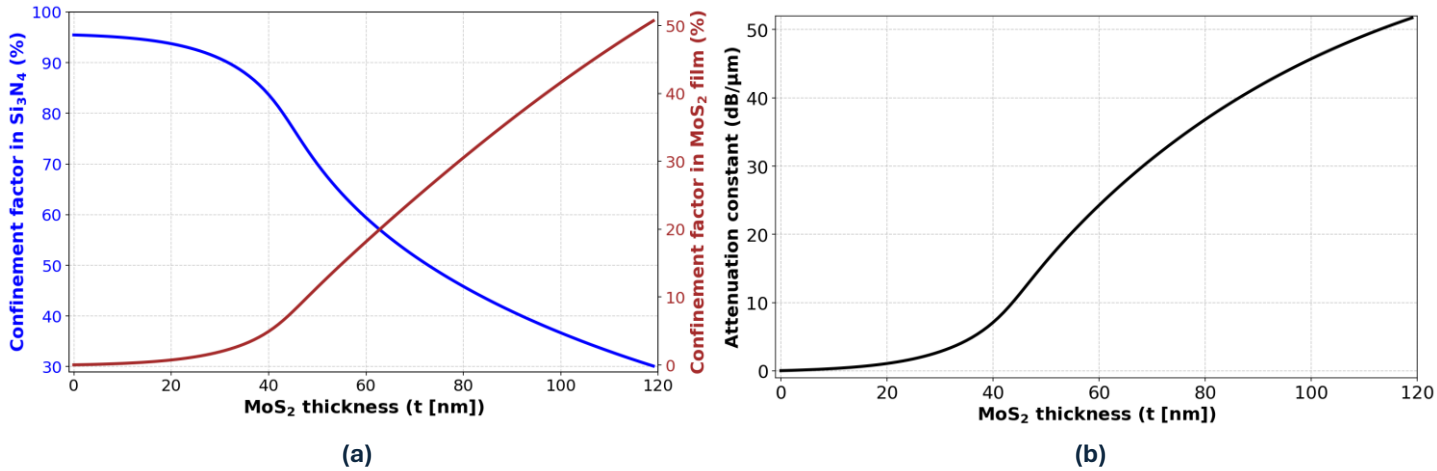

Figure S1c: As tabulated in Fig. S5b, the graphs in (a) shows the simulated confinement factors in the Si_3N_4 waveguide core and MoS_2 film as a function of MoS_2 film thickness (b) shows the corresponding increase in attenuation constant (dB/μm), indicating light absorption in thicker MoS_2 layers.

S2: Raman characterization of MoS_2 flake.

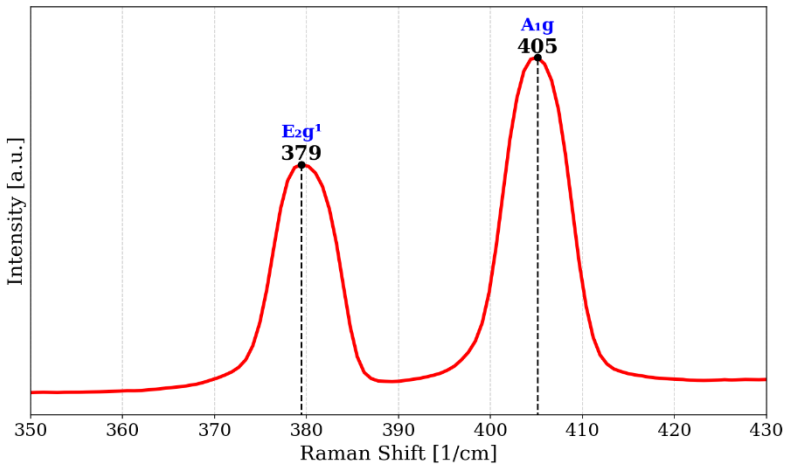

Fig. S2: Raman response of MoS_2 flake transferred onto a Si_3N_4 waveguide: *The two distinct peaks at ~379 cm^{-1} and* ~405 cm^{-1} correspond to the E_2g^1 (in-plane vibrational mode) and A_1g (out-of-plane vibrational mode) of the MoS_2 flake, respectively. The vertical black dashed lines mark the peak positions for clarity, and the peak separation (~26 cm^{-1}) indicates a multilayer MoS_2.

S3: AFM of MoS_2 flakes transferred on the waveguides.

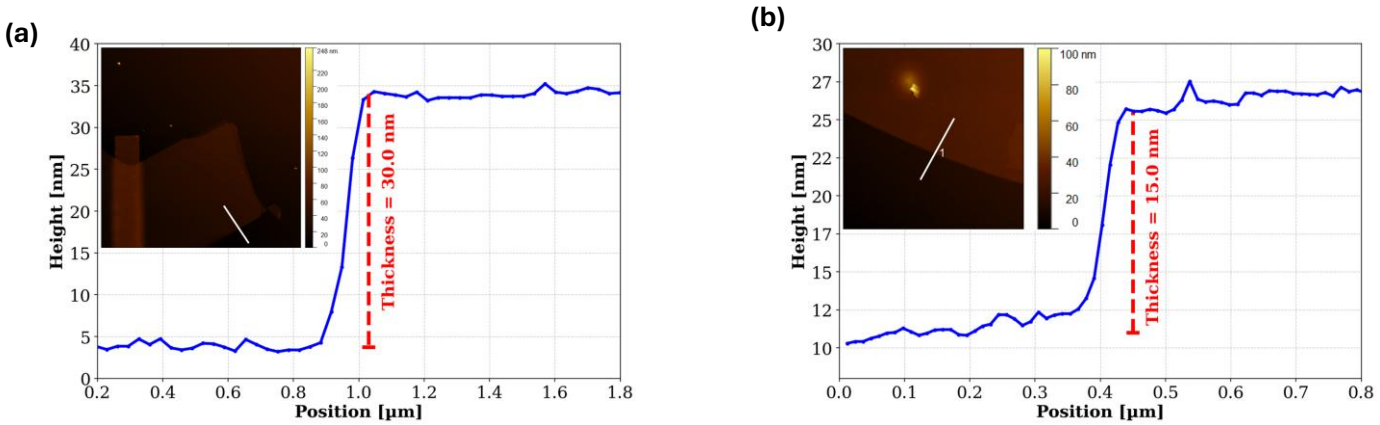

Fig. S3: Atomic Force Microscopy (AFM) height profiles of MoS_2 flakes in different structural configurations. (a) shows the MoS_2 flake on a straight waveguide with a measured thickness of 30 nm, while (b) shows the MoS_2 flake on a coiled waveguide structure with a thickness of 15 nm. The lateral axis corresponds to the white line drawn across the flakes in the insets. The measurements confirm the multilayer nature of the flakes used in the electro-optical characterization.

S4: Waveguide characterization setup and transmission loss measurements of silicon-nitride waveguides.

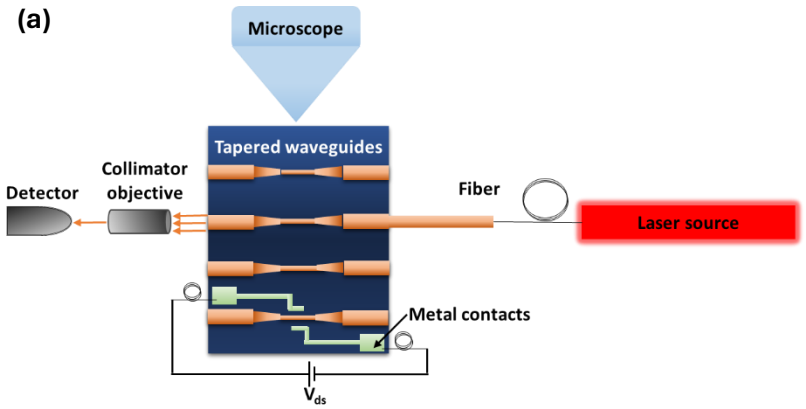

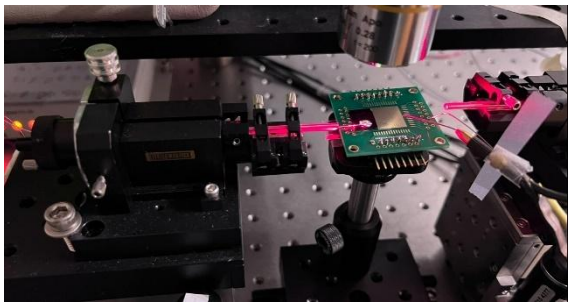

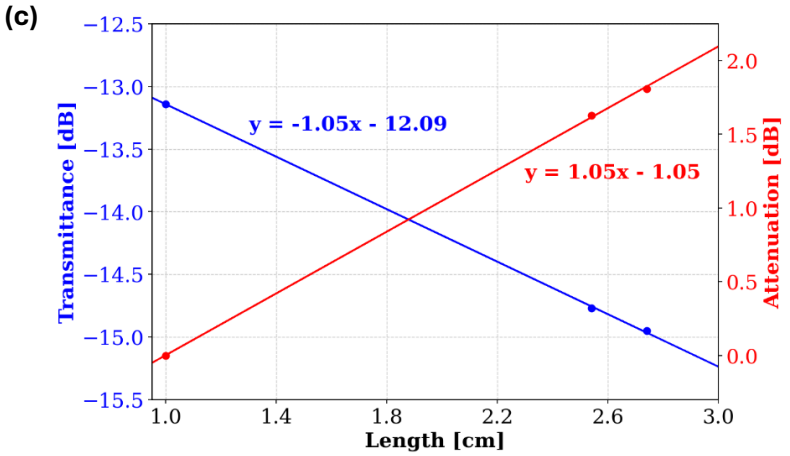

(d)

Laser Output Power [µW]	Estimated Power at Photodetector [µW]
147.74	7.20
96.65	4.71
75.92	3.70
35.49	1.72
1.03	0.05
0.41	0.02

Fig. S4: Top-view illustration and image of custom-built waveguide characterization setup with the optical transmittance and attenuation measurements as functions of propagation length in a waveguide.

An optical fiber of 2 µm was used to inject light in a 3 µm tapered waveguide, as shown in **(a)**. The tapered waveguides are used both at the input and output to ease light coupling. The output light is collimated by an objective lens and detected by the power meter or output camera to observe the optical mode. A top-view microscope was employed to align the fiber and waveguide for optimal light propagation in the waveguide, while metal contacts were used to enable the electrical measurements in 2D material. The experimental setup captured in **(b)** validates the successful light coupling into the waveguide and device. The transmittance and attenuation measurements graphs shown in **(c)** illustrate the relationship between detected output power and the change in waveguide length. The cut-back method was employed to determine the losses by varying the length of the waveguides. A linear fit to the data was applied and extrapolated, and an insertion loss of ~12.09 dB was obtained, while the propagation loss was ~1.05 dB/cm. Low propagation and moderate insertion loss indicate efficient light transmission to the photodetector, which enhances light-matter interactions. **(d)** Table showing the measured laser output from the laser source and the actual power reaching the photodetector using the transmittance loss equation in S3c.

S5: Photocurrent generated by a MoS_2 on a straight waveguide and a MoS_2 on a coiled waveguide structure.

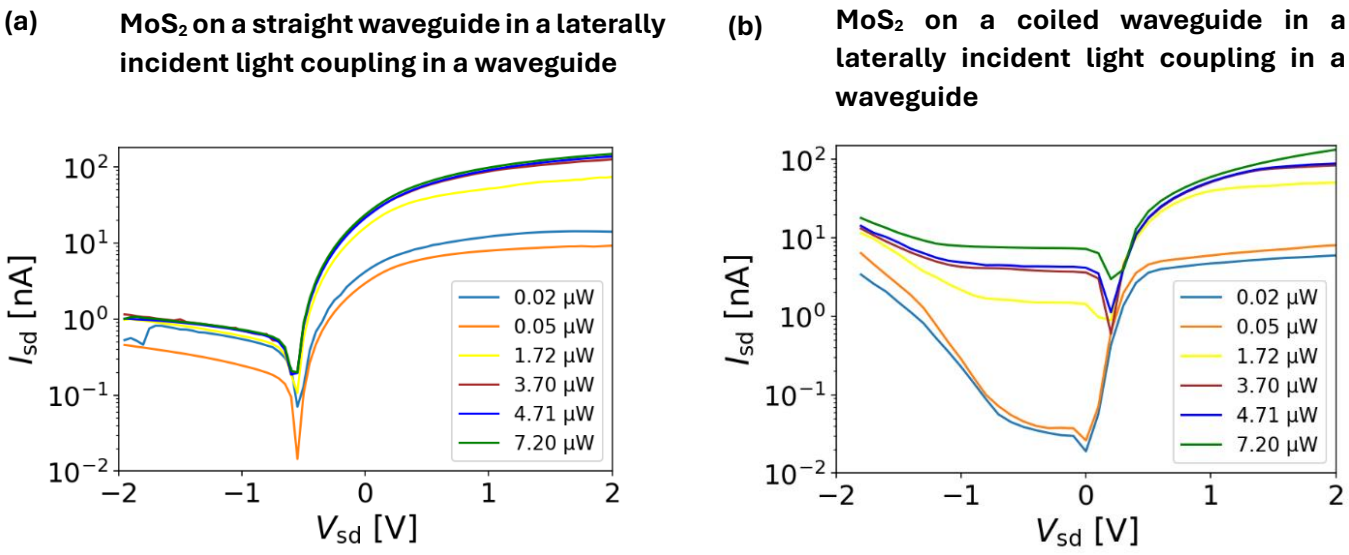

Figure S5: Photocurrent generated in MoS_2 integrated on (a) a straight waveguide and (b) a coiled waveguide under lateral light coupling at varying optical powers. The photocurrent increases with optical power in both configurations, with a steeper slope in the coiled waveguide structure. The light propagates through the waveguide and generates an electric field perpendicular to the waveguide plane, enabling light-matter interaction with MoS_2.

S6: Dark current of MoS_2 flakes on a straight and coiled waveguide structures.

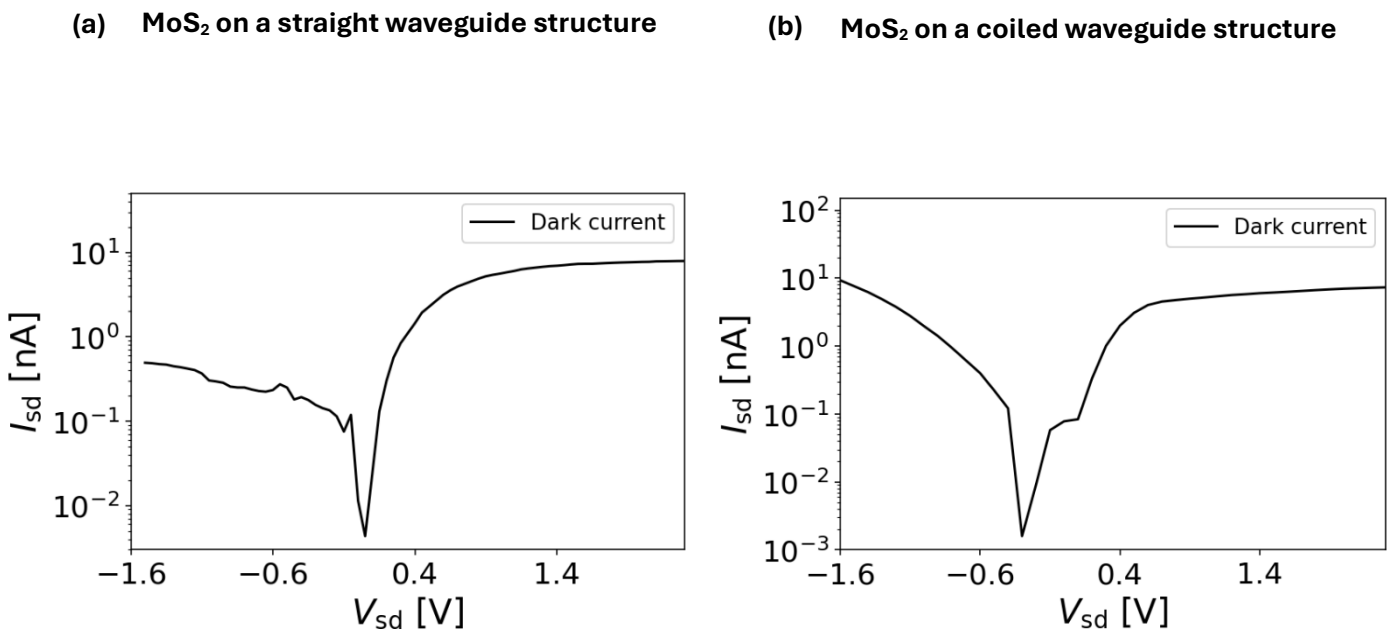

Figure S6: Dark current characteristics of MoS_2 flakes integrated on a (a) straight waveguide and (b) coiled waveguide structure. The coiled geometry enables a longer interaction length, resulting in improved carrier transport effects. Both structures demonstrate asymmetric current-voltage behavior under dark conditions.

S7: Gate voltage curve of MoS_2 flakes on a coiled waveguide structure.

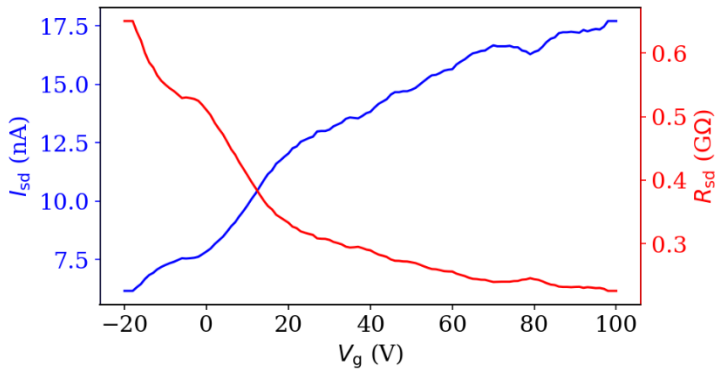

Figure S7: Gate-dependent source–drain current I_{sd} and resistance R_{sd} of the coiled MoS_2 photodetector.

Fig. S8: Simulated mode profile of a single layer MoS_2 film, transmittance, absorption and top-view field evolution in a Si_3N_4 waveguide with an overlaid MoS_2 layer of varying interaction length.

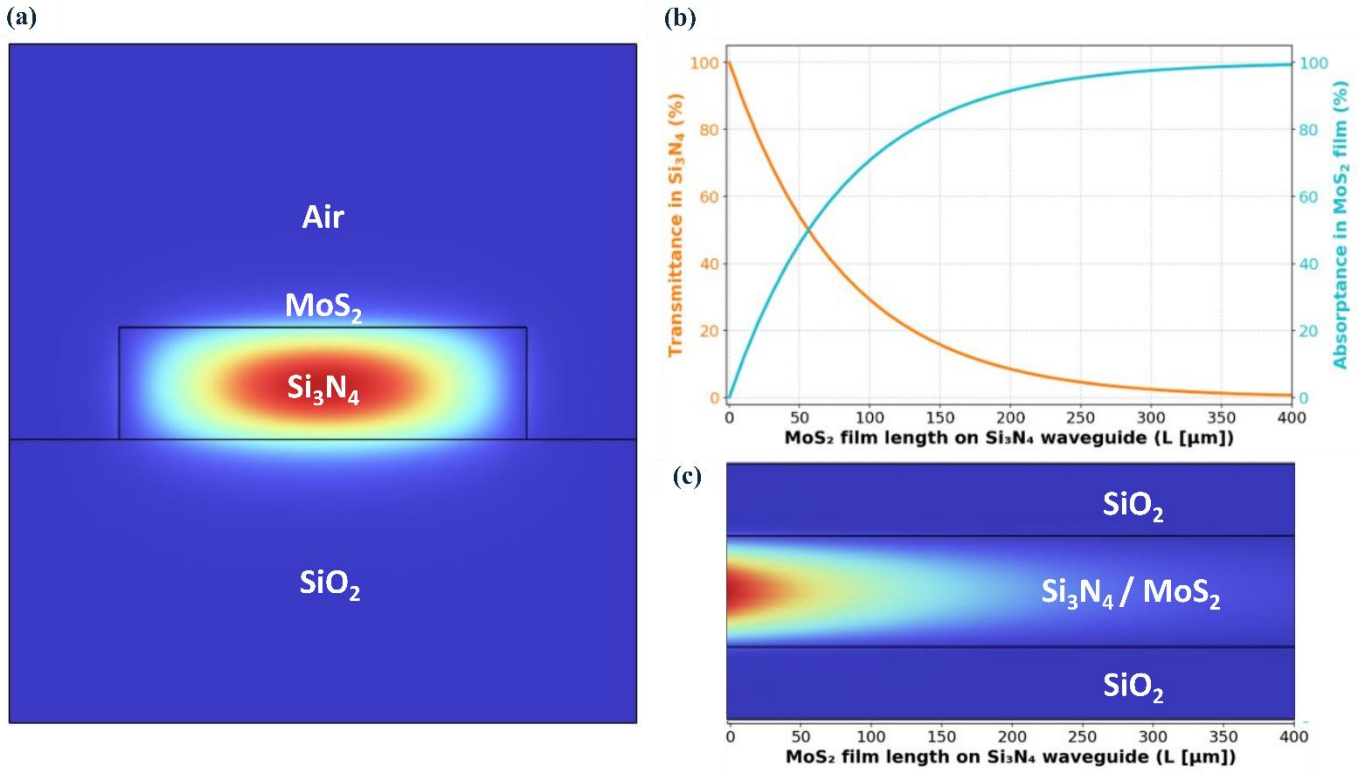

Figure S8: (a) Simulated optical mode profile of a Si_3N_4 waveguide covered with a monolayer (0.65 nm) MoS_2 film, showing evanescent coupling into the 2D material. (b) Variation of transmittance and absorptance as the interaction length increases up to 400 nm, highlighting that a substantial length is required for significant absorption when using a single MoS_2 layer. (c) Top-view simulation illustrating the gradual attenuation of the optical mode along the waveguide due to interaction with the monolayer MoS_2. These results highlight the critical role of extending the light-matter interaction length, achievable through compact coiled waveguide designs, in boosting optical absorption and responsivity when utilizing atomically thin 2D materials.

Fig. S9: Simulated optical absorptance in MoS_2 on a straight and coiled waveguides.

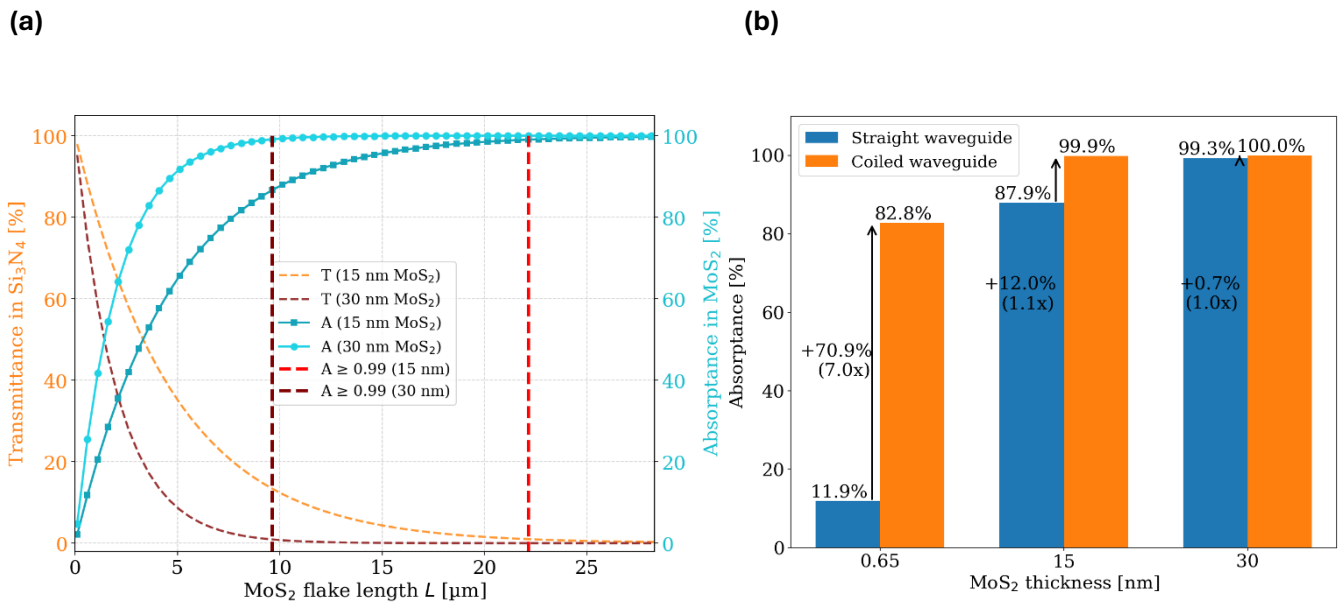

Figure S9. (a) Simulated transmittance and MoS_2 absorptance at 532 nm versus flake length for 15 nm and 30 nm films. (b) Total MoS_2 absorptance for straight and coiled waveguides at 0.65 nm, 15 nm and 30 nm thickness, highlighting the stronger absorption provided by the coiled geometry, especially for ultrathin MoS_2.

Fig. S10: Benchmark comparison of our waveguide-integrated coiled MoS_2-based photodetectors with previous photodetectors made with similar 2D materials.

Device materials	Material thickness	Device architecture	Incident Wavelength [nm]	Vg / Vsd	Responsivity [A/W]	Reference
MoS_2	30 nm	Waveguide-integrated	532	2 V	0.61	This work
MoS_2	60 nm	Waveguide-integrated	1550	1 V	1.05	[1]
MoS2	Not specified	Non-waveguide-integrated	1550	2 V	34	[2]
MoS_2/Au	3 nm	Waveguide-integrated	1550	5 V	0.3	[3]
MoS2	0.65 nm	Non-waveguide-integrated	561	-70V/ 8V	0.88	[4]
MoS2	0.65 nm	Waveguide-integrated	647	0 V / 1 V	1000	[5]
TaSe2-MoS2-graphene	0.7 nm	Non-waveguide-integrated	532	0 V / 0.2 V	10	[6]
Graphene- MoS2	1 nm	Waveguide-integrated	532	30 V / 0 V	0.44	[7]
Graphene-MoS_2 heterostructure	0.65 nm / 3 nm	Waveguide-integrated	520	1 V	10^7	[8]
MoS2-InSe	242 nm / 107 nm	Waveguide-integrated	532	-60V/ 2V	0.11	[9]
GQDs/InSe	Not specified	Non-waveguide-integrated	635	Not specified	27.48	[10]
MoTe2/graphene	Not specified	Non-waveguide-integrated	1310	Not specified	0.567	[11]
MoSe2-WS2	20 nm / 1 nm	Waveguide-integrated	780	0 V / 2 V	0.97	[12]
MoSe2-WS2	20 nm / 1 nm	Waveguide-integrated	780	0 V / 2 V	0.97	[13]
BP-MoTe2	13 nm/ 10.6 nm	Waveguide-integrated	1503	0 V / 0 V	0.27	[14]
MoTe2	60 nm	Waveguide-integrated	1550	0 V / -2 V	0.50	[15]
Graphene	0.37 nm	Waveguide-integrated	1550	3.2 V / -0.3 V	0.40	[16]
Black phosphorus	40 nm	Waveguide-integrated	2000	0 V / 0.4 V	0.31	[17]

References

[1] F. Yang, Y. Hu, J. Ou, Q. Li, X. Xie, H. Han, C. Cai, S. Ruan, B. Xiang, *ACS Photonics*, DOI: 10.1021/acsphotonics.4c02618.

[2] X. Liu, J. Zhu, Y. Shan, C. Liu, C. Pan, T. Zhang, C. Liu, T. Chen, J. Ling, J. Duan, F. Qiu, S. Rahman, H. Deng and N. Dai, *Advanced Science*, DOI:10.1002/advs.202408299.

[3] C. Hong, S. Oh, V. K. Dat, S. Pak, S. N. Cha, K. H. Ko, G. M. Choi, T. Low, S. H. Oh and J. H. Kim, *Light Sci Appl*, DOI:10.1038/s41377-023-01308-x.

[4] O. Lopez-Sanchez, D. Lembke, M. Kayci, A. Radenovic and A. Kis, Nat Nanotechnol, 2013, 8, 497–501.

[5] J. F. Gonzalez Marin, D. Unuchek, K. Watanabe, T. Taniguchi and A. Kis, NPJ 2D Mater Appl, DOI:10.1038/s41699-019-0096-4.

[6] M. Mahajan, S. Kallatt, M. Dandu, N. Sharma, S. Gupta and K. Majumdar, Commun Phys, DOI:10.1038/s42005-019-0190-0.

[7] Z. Wu, T. Zhang, Y. Chen, Y. Zhang and S. Yu, Physica Status Solidi - Rapid Research Letters, 2019, 13.

[8] W. Zhang, C. Chuu, J. Huang, C. Chen, M. Tsai, Y. Chang, C. Liang, Yu. Chen, Yu. Chueh, Jr. He, Mei. Chou, Lain, Li, *Scientific Reports*, DOI: 10.1038/srep03826.

[9] X. Cui, M. Du, S. Das, H. H. Yoon, V. Y. Pelgrin, D. Li and Z. Sun, Nanoscale, DOI:10.1039/d2nr01042a.

[10] S. R. Tamalampudi, J. E. Villegas, G. Dushaq, R. Sankar, B. Paredes and M. Rasras, Adv Photonics Res, DOI:10.1002/adpr.202300162.

[11] C. Yang, Z. Liu, H. Cai, D. Li, Y. Yu, X. Zhang, *ACS Photonics*, DOI:10.1021/acsnano.4c14937.

[12] R. Gherabli, S. R. K. C. Indukuri, R. Zektzer, C. Frydendahl and U. Levy, Light Sci Appl, DOI:10.1038/s41377-023-01088-4.

[13] N. Flöry, P. Ma, Y. Salamin, A. Emboras, T. Taniguchi, K. Watanabe, J. Leuthold and L. Novotny, Nat Nanotechnol, 2020, 15, 118–124.

[14] R. Tian, X. Gan, C. Li, X. Chen, S. Hu, L. Gu, D. Van Thourhout, A. Castellanos-Gomez, Z. Sun and J. Zhao, Light Sci Appl, DOI:10.1038/s41377-022-00784-x.

[15] R. Maiti, C. Patil, M. A. S. R. Saadi, T. Xie, J. G. Azadani, B. Uluutku, R. Amin, A. F. Briggs, M. Miscuglio, D. Van Thourhout, S. D. Solares, T. Low, R. Agarwal, S. R. Bank and V. J. Sorger, Nat Photonics, 2020, 14, 578–584.

[16] J. Guo, J. Li, C. Liu, Y. Yin, W. Wang, Z. Ni, Z. Fu, H. Yu, Y. Xu, Light Sci Appl, DOI:10.1038/s41377-020-0263-6.

[17] Y. Yin, R. Cao, J. Guo, C. Liu, J. Li, X. Feng, H. Wang, W. Du, A. Qadir, H. Zhang, Y. Ma, S. Gao, Y. Xu, Y. Shi, L. Tong, D. Dai, Laser & Photonics Reviews, DOI: 10.1002/lpor.201900032.